Effect of shear on coherent structures in turbulent convection

Prafulla P. Shevkar
Department of Applied Mechanics
Indian Institute of Technology Madras, Chennai, India 600036

G. S. Gunasegarane
Department of Mechanical Engineering,
Pondicherry Engineering College,
Pillaichavadi, Puducherry, India, 605014

Sanal K Mohanan and Baburaj A. Puthenveettil*
Department of Applied Mechanics
Indian Institute of Technology Madras, Chennai, India 600036
(Dated: January 8, 2019)

We study the effect of shear on the structure of plumes near the hot surface in turbulent Rayleigh Benard convection (RBC) and turbulent mixed convection for the range of near surface Rayleigh numbers $5.75 \times 10^7 \leq Ra_w \leq 6.03 \times 10^8$ and shear Reynolds numbers $8.02 \times 10^2 \leq Re \leq 15 \times 10^3$ for a Prandtl number range of $5.24 \geq Pr \geq 0.7$ in water and air. Plumes are visualised by particle scattering in mixed convection in air while they are extracted from the PIV fields in RBC in water. The planforms of plume structure show that shear aligns the line plumes and increases their mean spacing λ. An increase in Ra_w decreases the mean plume spacing while the resulting increase in Re in RBC, due to the increase of larger large scale flow strength, counteracts this effect. Further, the plumes are seen more spaced and smeared in air compared to that in water due to the lower Pr. We show that these complex dependences of the plume spacing on Ra_w, Re and Pr in RBC and mixed convection can be described by a common scaling law of λ on the shear parameter $S = Re^3/Ra_w$ and Pr.

I. INTRODUCTION

In turbulent Rayleigh Benard convection (RBC), line plumes are the predominant coherent structures that originate in the diffusive regions near the hot surface. These line plumes form, merge and rise, resulting in a complex network of lines on the hot surface, which essentially act as channels transporting heat from the diffusive regions near the plate to the fully turbulent bulk. Since the majority of the heat from the hot plate is transported by these coherent structures [1], understanding the scaling of their geometry is essential in understanding the phenomenology of flux scaling in turbulent convection.

These lines plumes are the outcome of the gravitational instability of the local natural convection boundary layers [2] that form on the hot surface; the spacings between them are then indicative of the length at which these local boundary layers become unstable. In the absence of predominant shear, these spacings are distributed lognormally at any instant [3, 4], with the mean plume spacing in the absence of shear, scaling as

$$\lambda_0 = C_1 Pr^{n_1} Z_w, \tag{1}$$

as given by Puthenveettil et al. [5]. Here,

$$Z_w = \left(\frac{\nu\alpha}{g\beta\Delta T_w}\right)^{1/3} = \frac{H}{Ra_w^{1/3}} \tag{2}$$

is a length scale near the plate [6, 7], with the subscript 0 indicating the no-shear values hereinafter. The near surface Rayleigh number $Ra_w = g\beta\Delta T_w H^3/\nu\alpha$, with ν being the kinematic viscosity, α the thermal diffusivity, β the coefficient of thermal expansion, ΔT_w the temperature drop between the hot plate and the bulk and H, the layer height. The Prandtl number $Pr = \nu/\alpha$, $C_1 = 47.5$ and $n_1 = 0.1$. The relation (1) also implies that

$$Ra_{\lambda_0}^{1/3} = C_1 Pr^{n_1}, \tag{3}$$

where $Ra_{\lambda_0} = g\beta\Delta T_w \lambda_0^3/\nu\alpha$ is the Rayleigh number based on λ_0. Since the total length of plumes L_p over an area A of the hot plate is $L_p = A/\lambda_0$, Puthenveettil et al. [5] show that (1) and (2) also imply that

$$\frac{L_p}{A/H} = \frac{Ra_w^{1/3}}{C_1 Pr^{n_1}}. \tag{4}$$

The same scaling, without Pr dependence, has also been obtained by [8], who connected it empirically to the volume averaged Kolmogorov length.

At higher Ra_w, these line plumes organise themselves to create a large scale flow, which then change the flux scaling from the classical $Nu \sim Ra^{1/3}$ scaling law, where Nu is the Nusselt number and the Rayleigh number $Ra = 2Ra_w$. This anomalous flux scaling is expected to be due to the modification of the boundary layers by the shear due to the large scale flow. The nature of this modification is still not clear, with the popular theory of Grossman and Lohse[9] assuming that the boundary layers become Blasius boundary layers due to the shear of the large scale flow, which however has not been observed [10, 11]. Similar modification of boundary layers due

* apbraj@iitm.ac.in

to shear is expected in mixed convection (MC) where the shear is provided by an externally imposed horizontal mean flow. Studies abound on the heat flux scaling in mixed convection, where an empirical summation of the power law scalings in the limiting cases of forced convection and free convection are often used [12–15]. Since the heat flux is mostly transported by plumes, these changes in the flux scaling with shear in RBC and MC, whose phenomenology is still not clear, could also be expected to alter the structure of the line plumes on the hot surface with shear.

Quantitative knowledge about such changes to the plume structure with shear, in terms of the changes in the spacings between the line plumes, is however limited. Various visualisations in RBC [3, 16] and MC, [13, 15, 17, 18] show that shear aligns the line plumes along the shear direction. In both these cases, it is however not known whether shear changes the spacings between these coherent structures, and if it changes, how much that change will be from that given by (1) for the case of no predominant shear. No knowledge of the scaling of spacings with ΔT_w and shear velocity U_{sh}, or on the corresponding dimensionless parameters Ra and the shear Reynolds numbers $Re = U_{sh}H/\nu$ is available. Since these coherent structures carry most of the heat from the hot surface[1], such a knowledge about changes in the nature of the plume structure with shear could be crucial in understanding the shear engendered, anomalous, heat flux scaling in turbulent convection. Such a knowledge could also lead to ways to improve the heat transfer from surfaces by manipulating these structures. Further, the geometry, organisation and dynamics of these coherent structures are of interest in the overall phenomenology of turbulent RBC and MC, like the importance of coherent near wall vortices in shear turbulence[19]. In addition, the knowledge about the spacing and length of these line plumes could also lead to effective wall functions for modelling of turbulent RBC and MC, as has been done in shear turbulence [20, 21].

In the present study, we study the effect of shear on the spacing between the coherent line plumes on the hot surface in steady turbulent Rayleigh Benard convection in water ($Pr = 5-6$) as well as in steady turbulent mixed convection in air ($Pr = 0.7$). We also include the spacings measured from the planforms of Gilpin et al. [17] for mixed convection experiments in water ($Pr = 10.1$) and from the mixed convection simulations of Pirozzoli et al.[15] at $Pr = 1$ to conduct the analysis over a two decade range of Rayleigh numbers, $5.0\times10^7 \leq Ra_w \leq 2.17\times10^9$. The shear in our experiments is imposed externally in air, while in water, it is internally generated due to the large scale flow to create about two orders of shear Reynolds numbers, $802 \leq Re \leq 15000$. We show that shear aligns the line plumes in the direction of the shear, with a mean spacing that increases with shear at the same Ra_w. An increase in Ra_w decrease the spacing at the same shear, with the spacings being a function of Pr also. This complex dependence of the spacing of line plumes on Ra_w, Re and Pr is then shown for a given fluid to only depend on a shear parameter $S = U_{sh}^3\alpha/g\beta\Delta T_w\nu^2$, which reflects the relative strength of shear with respect to buoyancy and dissipative effects.

II. EXPERIMENTS

A. Setup and procedure

1. Mixed convection experiments with air

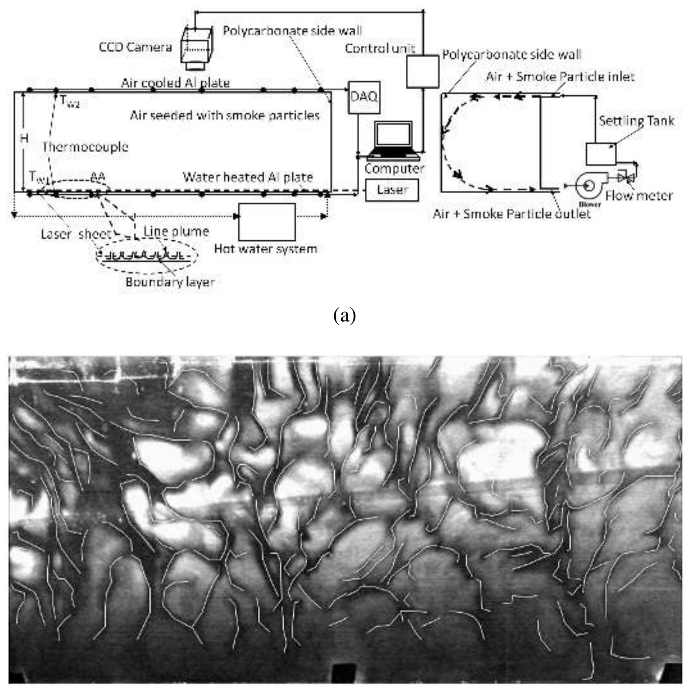

(a)

(b)

FIG. 1. (a),Schematic of the setup for steady mixed convection experiments in air at $Pr = 0.7$; (b), Line plumes marked with short linear segments in the planform obtained at $Ra_w = 1.55\times10^8$ and external flow rate $Q = 1736$ lpm.

The schematic of the convection cell that had an area of cross section 2.5m $\times$0.5m, used for steady state temperature driven convection experiments in air at $Pr = 0.7$ with an imposed external flow, is shown in figure 1(a). The top and bottom aluminium plates were separated by four transparent polycarbonate side walls of height $H = 0.5$m. The bottom aluminium plate was maintained at a constant temperature using a temperature controlled water circulating system while the top plate was air cooled by fans so that a constant mean temperature difference ΔT between the plates could be maintained. A flow of air was externally imposed through an inlet of height 25 mm at the top of one of the side walls and an outlet of height 15 mm at the bottom on the same side wall that extended over the entire length of the convection cell. The external flow was allowed to settle for nearly 60 minutes before taking the measurements.

ΔT was determined from spatial and temporal averaging of the plate temperatures recorded at 25 locations in each plate using PT100 resistance thermometers. The temperatures of the incoming and the outgoing air were measured using PT100 temperature sensors placed equidistantly over

TABLE I. Experimental parameters, dimensionless numbers and the plume spacings in the present study. ×, MC experiments by Gilpin et al. [22]; ✳, MC simulations by Pirozoli et al. [15].

Symbol	Type	Fluid	Pr	ΔT_w °C	H mm	Q lpm	U_{sh} mm/s	λ mm	Ra_w $\times 10^8$	Re $\times 10^3$
○	MC	Air	0.7	4.41	500	1087	290	49.3	0.575	9.577
						1167	311	56.2	0.575	10.28
						1249	333	64.9	0.575	10.997
□	MC	Air	0.7	7.95	500	1267	338	44.84	1.01	11.068
						1399	373	48.18	1.01	12.214
						1436	383	55.03	1.01	12.542
◇	MC	Air	0.7	9.88	500	1417	398	41.78	1.24	12.333
						1500	400	46.1	1.24	13.051
						1601	427	51.84	1.24	13.932
△	MC	Air	0.7	12.56	500	1537	410	40.11	1.55	13.283
						1676	447	43.33	1.55	14.482
						1736	463	47.93	1.55	15.0
●	RBC	Water	5.24	2.59	120		5.2	15.5	1.09	0.802
							5.4	15.6	1.09	0.832
							6.1	15.6	1.09	0.94
■	RBC	Water	5.18	3.27	150		8.8	15.4	2.79	1.717
							9.4	16.7	2.79	1.834
							10.0	15.8	2.79	1.951
♦	RBC	Water	5.09	4.58	175		10.8	17.2	6.03	2.49
							12.3	15.1	6.03	2.836
							13.4	16.3	6.03	3.09
×	MC	Water	10.1	11.5	457		29	23.84	21.7	9.573
✳	MC	Simulations	1	5	855		261	131.3	0.5	10

the entire length of the cell. The maximum possible error in temperature measurement was 0.25°C. External circulation flow rates ranging from $Q = 1087$ to 1736 lpm, at different ΔT maintained between the conducting plates, were used. These flow rates correspond to the mean shear velocities of air entering and leaving the convection cell over the range 0.29 m/s$\leq U_{sh} \leq$ 0.463 m/s corresponding to a Reynolds number range of $9577 \leq Re \leq 15000$. The range of Rayleigh numbers in these experiments, $5.75\times10^7 < Ra_w < 1.55\times10^8$, was obtained by changing ΔT over the values shown in Table I.

2. *RBC experiments with water*

Steady turbulent Rayleigh-Benard convection (RBC) experiments in a water layer, confined between a hot copper plate at the bottom and a water cooled glass plate at the top, were carried out in a glass tank of cross-section 30 cm ×30 cm, with insulated side walls, in the setup shown in the figure 2. The bottom copper plate was maintained at a constant heat flux by a heater plate assembly connected to a variac. The heat flux was estimated from the measured temperature drop across a glass plate in the plate assembly by T-type thermocouples at three different locations. The temperatures of the hot Cu plate (T_h) and the cold glass plate (T_c) were measured at two different locations by T-type thermocouples, whose average was used to calculate the constant temperature difference of $\Delta T = T_h - T_c$. The error in temperature measurement was $0.02°C$. Experiments were conducted over the range of Ra_w and Pr shown in table I, obtained by changing the variac voltage, the layer height H and the water flow rate over the cooling plate.

The velocity fields in $x-y$ plane at a height h_m, which was less than the Prandtl-Blasius boundary layer thickness (δ_{pb}) [23] and the natural convection boundary layer thickness (δ_{nc}) [5], were obtained by stereo PIV. The flow was seeded with poly-amide particles (mean diameter d_p = 55 μm and density ρ_p = 1.012 g cm^{-3}) and illuminated by a 1mm thick horizontal laser sheet from a Nd: YAG laser (Litron, 100 mJ/pulse); the particles followed the flow since the Stokes number was less than 0.00415. The laser pulse separation was chosen so that the particle displacement was not more than

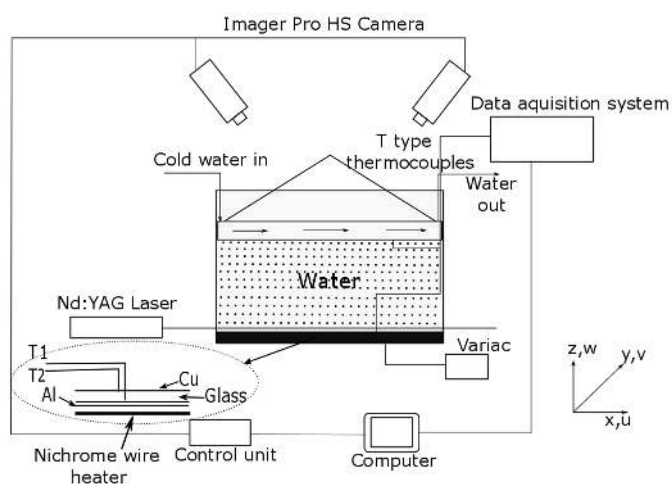

FIG. 2. Schematic of the experimental setup for steady RBC in water

TABLE II. Parameters for the PIV measurements in water. Physical properties were estimated at T_B, the bulk fluid temperature.

Ra_w	T_B (° C)	h_m (mm)	δ_{pb} (mm)	δ_{nc} (mm)	A_i (mm^2)	Δt (s)	D_I (pix)	overlap %	spatial resolution (mm)
1.09×10^8	31.42	1.5	11.1	2.2	83.08×71.94	0.0667	32	50	1.04
2.79×10^8	31.88	1.0	8.9	2.0	82.28×70.38	0.0667	32	50	1.03
6.03×10^8	32.60	1.3	7.5	1.8	84.10×73.86	0.0667	32	50	1.05

the one-fourth of the laser sheet thickness. Two Imager Pro HS cameras (LaVision GmbH, 1024 × 1280 pixels), oriented at 32.5° with the vertical, with depth of field more than the laser sheet thickness, were used to capture the images at 15Hz at the center of the hot plate. The imaging areas A_i, shown in Table II, were chosen so that sufficient number of line plumes were present in A_i. Refraction errors were reduced by viewing the bottom plate through a water filled prism placed over the top cold chamber, the errors due to this oblique imaging were reduced by using a third order polynomial mapping function obtained by imaging a calibration plate.

A multipass adaptive window stereo cross correlation method (Davis®) was applied on images obtained this way, after high pass filtering, to calculate the 2D-3C vector field. The size of the interrogation window (D_I) and the particle concentration was chosen so that the displacement of particles $x_p \leq D_I/4$ and at least ten particles were present in an interrogation window at any time. Spurious vectors were removed by applying a median filter of 3pix × 3pix neighbourhood and gaps were filled by interpolation. Other relevant parameters of the PIV measurements are shown in table II, while two typical vector fields obtained at $Ra_w = 1.09 \times 10^8$ and 6.03×10^8 are shown in figure 3. Uncertainty in the estimated velocity in all the interrogation windows was calculated from the correlation statistics using the methodology of Wieneke [24], using Davis®. The maximum value of the mean uncertainty from all the images at the lowest and the highest Ra was 0.298 mm/s and 0.364 m/s respectively. These mean uncertainties are 4.9% and 3.4% of corresponding mean shear velocities at the corresponding Ra.

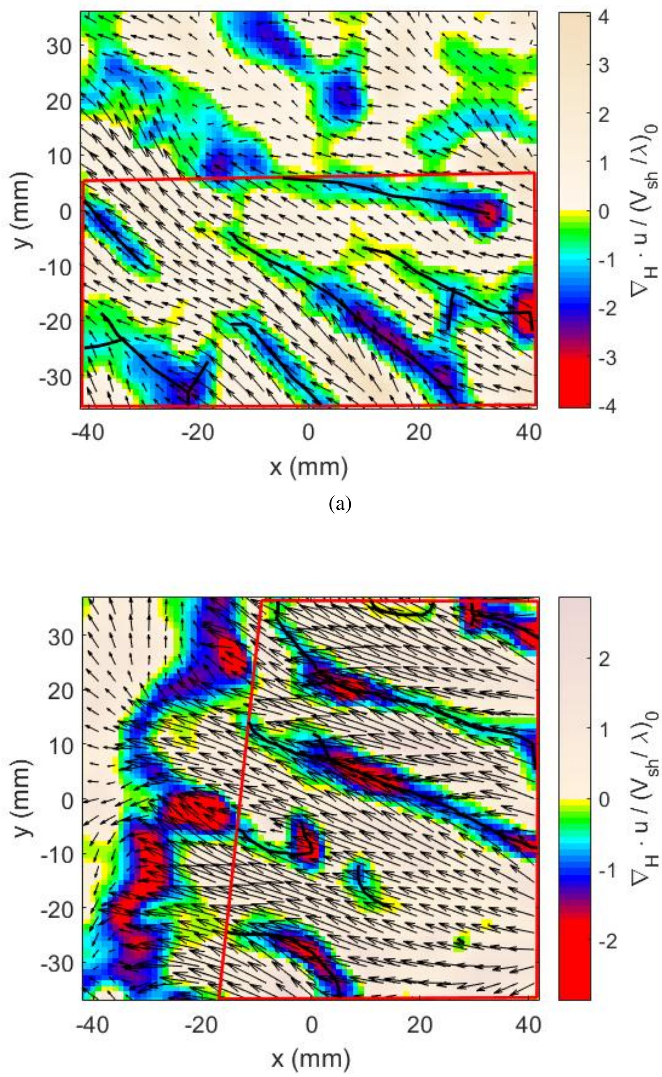

(a)

(b)

FIG. 3. Dimensionless horizontal divergence fields, overlaid over the horizontal velocity vector fields, in a horizontal plane at a height h_m from the hot surface in RBC in water. (a), $Ra_w = 1.09 \times 10^8$, $Re = 832$ and $h_m = 1.5$ mm; (b), $Ra_w = 6.03 \times 10^8$, $Re = 2490$ and $h_m = 1.3$ mm. Plumes are the colour regions. Shear dominant areas are shown by the red polygon. L_p is measured by adding up the length of the black lines in the plume regions.

B. Detection of plumes

In mixed convection experiments with air, the planforms of plume structures near the plate were made visible when a horizontal light sheet from a 532 nm Nd-Yag laser was scattered by the smoke particles injected into the external air flow circuit. The laser sheet was 2mm thick with its centreline at h_m = 4mm above the bottom hot plate. Since the plumes have relatively lesser number of smoke particles, possibly since the smoke particles have to get into the plumes through entrainment from the bulk or into the boundary layers, they scatter less light and hence appear as dark lines in a bright background. Figure 1(b) shows the planform of plume structure visualised in this way above the bottom horizontal plate at $Ra_w = 1.55 \times 10^8$. The thick darker lines in the image are the top view of the line plumes. The convection cell had a closed opaque top, the top views of the plume structures near the bottom plate were hence captured through the side walls by a CCD camera at 10fps. The perspective errors caused by this inclined camera axis were removed using a horizontal calibration plate in the plane of observation. Since all the plumes in the laser path will appear darker, no plumes are likely to be missed by this technique.

To detect plumes from the velocity fields obtained from PIV in the steady RBC experiments with water, we use the horizontal divergence criterion proposed by Vipin and Puthenveettil [25]. From the instantaneous horizontal divergence fields calculated from the horizontal velocity fields in a plane at height h_m, the criterion identifies regions with negative values as plumes. A 3pix $\times$3pix smoothing mean filter was applied to the vector field to reduce the noise while calculating divergence. Figure 3 shows the horizontal divergence fields, overlaid over the horizontal vector fields at two Ra_w; the coloured, line type regions show the plumes. We notice two types of regions in figures 3(a) and 3(b), (i) regions with smaller magnitudes of velocities where the line plumes are oriented in no particular direction and (ii) regions with larger magnitudes of velocities where the line plumes are aligned in the direction of these larger velocity vectors. To study the effect of shear on plume spacings, we estimate the plume spacings only in the regions where the plumes are aligned, and that have larger magnitudes of horizontal velocity. We estimate the average magnitude of horizontal velocity in such regions, shown by the red polygons in figure 3, and use this as the mean shear velocity U_{sh}.

We also measure the plume spacings from Gilpin et al.[17] and Pirozzoli et al.[15]. The plumes in Gilpin et al.[17] were visualised by the Phenolphathalene based electrochemical technique [26]. The technique causes colour changes to the dye only close to the hot surface, the dye with a different colour than the bulk near the hot plate then gets drawn into the plumes thereby making them visible. In the case of Pirozzoli et al. [15] plumes are identified as the regions with positive temperature fluctuations (T') from their given T' fields in a horizontal plane close to the hot surface (what height)?.

C. Measurement of plume spacing

Once the plumes are detected as described above, the mean plume spacing λ at each Ra_w and Re were estimated from the images by measuring the total plume length L_p in an area A and then using,

$$\lambda = A/L_p, \tag{5}$$

given by [5]. The plume lengths were measured from images similar to that in figure 3 and 4 by using a program that covers the plume lines with short linear segments on mouse clicks over the plume lines, which then calculates the total length of these lines. Figure 1(b) shows a planform in air at $Ra_w = 1.55\times10^8$ and 1736 lpm external flow, with the line plumes covered with such short linear segments, the sum of whose lengths give an estimate of L_p. Similarly, figure 3 shows two plan forms in water at $Ra_w = 1.09\times10^8$and 6.03×10^8, where the plumes are covered by line segments.

A possible error of 1.5% in λ was estimated from multiple measurements from the same planform in air. Similarly, for planforms in water, a 3% error in λ was estimated by measuring the maximum and minimum possible values of L_p from planforms. To estimate the error in the estimate of λ from Pirozzoli et al.[15], we estimate L_p from subregions in their figure 4(d) by marking segments in the red regions alone that show the highest values of T', and then in the red and yellow regions which show slightly lower values of T'. This process is repeated for different subregions to get a range of L_p, the error in λ is estimated from this range; the maximum possible error in λ was 2.9%. Error in the estimate of λ from Gilpin et al[17] was obtained by making multiple measurements of L_p from different subregions of the planform given in their figure 4(c) to give a maximum possible error of 4.3%. These values of errors in λ, or the errors derived using these values, are shown in the subsequent plots as the vertical error bars.

III. ANALYSIS OF MEAN PLUME SPACINGS

A. Qualitative analysis

Figure 4 shows the planforms in mixed convection in air at $Ra_w = 1.55\times10^8$ at Re of 13283, 14482 and 15000. The direction of external shear is from top to bottom in these figures. The planforms show that with increase in shear the plumes are distributed more uniformly, with the plumes becoming more aligned in the direction of shear. It also appears that the mean plume spacing increases in figure 4(c) compared to that in figure 4(a). Similar increased uniformity of spacing, increased alignment in shear direction and larger mean plume spacing with increasing shear were also observed in the planforms in air at the other Ra_w shown in table I. Since the spacing between the plumes is directly proportional to the distance over which the boundary layer between the plumes develop, before becoming unstable, it is hence clear that shear changes the stability of the local boundary layers between the plumes in turbulent convection. Figure 5 shows the planforms of plume structure at approximately the same Re of 10997 and 11068 but at different Ra of 5.75×10^7 and 1.01×10^8. It is clear that the density of plumes increases with increase in Ra resulting in smaller plume spacing with increase in Ra.

The plume structure at the centre of the bottom hot plate in steady RBC in water at $Ra_w = 1.09\times10^8$ and 6.03×10^8 is shown in Figure 3. Unlike in the case of mixed convection planforms in figures 4(a) to 4(c), where the effect of shear is seen to approximately align the plumes over the whole of the planform, here we notice that there are regions that show alignment of plumes, which are marked by the red polygon, while there are also regions in which the plumes are oriented randomly. The aligned plumes occur in regions with higher horizontal velocity magnitudes, as could be noticed by the larger velocity vectors in these regions in figures 3(a) and 3(b). As seen in table I, Re based on the average shear velocity U_{sh} in these regions are an order lower than the corresponding Re in figures 4(a) to 4(c). The shear is lower in the case of RBC experiments in water since shear is created by the self gener-

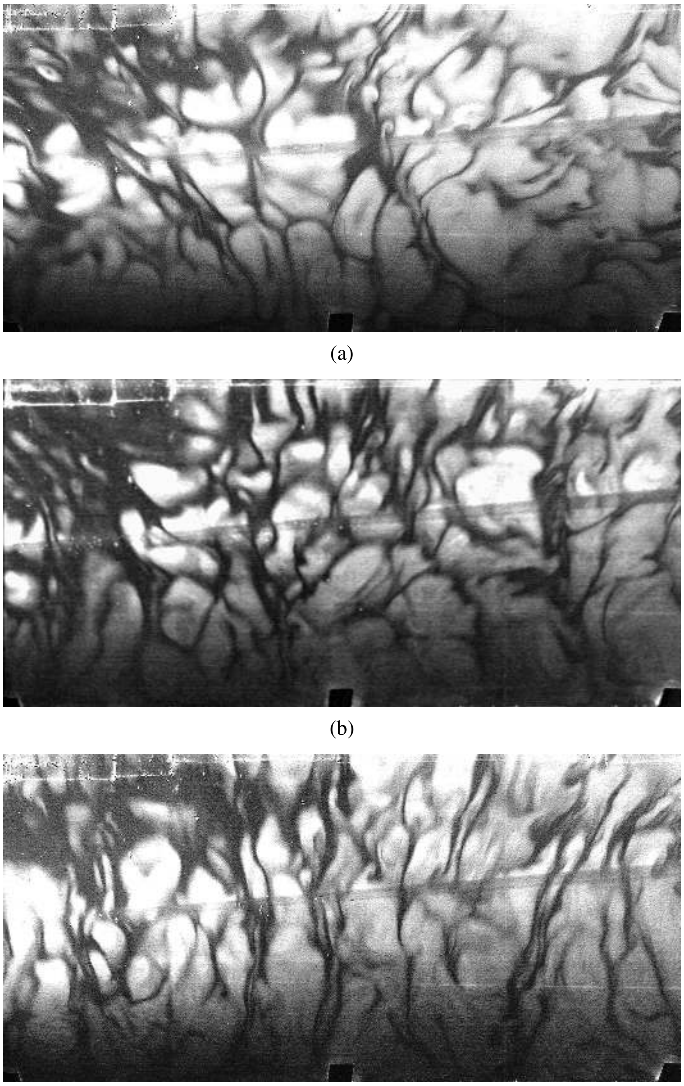
(a)
(b)
(c)

FIG. 4. Planforms of plume structure in mixed convection in air at $Ra_w = 1.55 \times 10^8$. (a), $Re = 13.28 \times 10^3$; (b), $Re = 14.48 \times 10^3$ and ; (c), $Re = 15 \times 10^3$. Flow is from top to bottom.

ated large scale flow at a higher Pr than in air, where the shear is externally forced. Such a lower shear in water experiments could be the reason for the splitting of the planforms into shear dominant and shear free regions in figure 3. In corroboration with this observation, we also observe that the extent of regions with aligned plumes increases with increase in Ra_w in these RBC experiments, since the large scale flow strength increases with increase in Ra_w. Since the planforms in figure 3 are over an area of 53 cm^2 while that in figure 4 are over an area of 6250 cm^2 the density of plumes are much more at the same Ra_w in water compared to that in air; increase in Pr hence seems to decrease the mean plume spacing. Unlike seen in the case of planforms in air in figure 4, in the planforms in water in figure 3, an increase of plume spacing in the shear dominant regions, compared to that in the low shear regions, or an increase in plume density with increase in Ra_w, are not

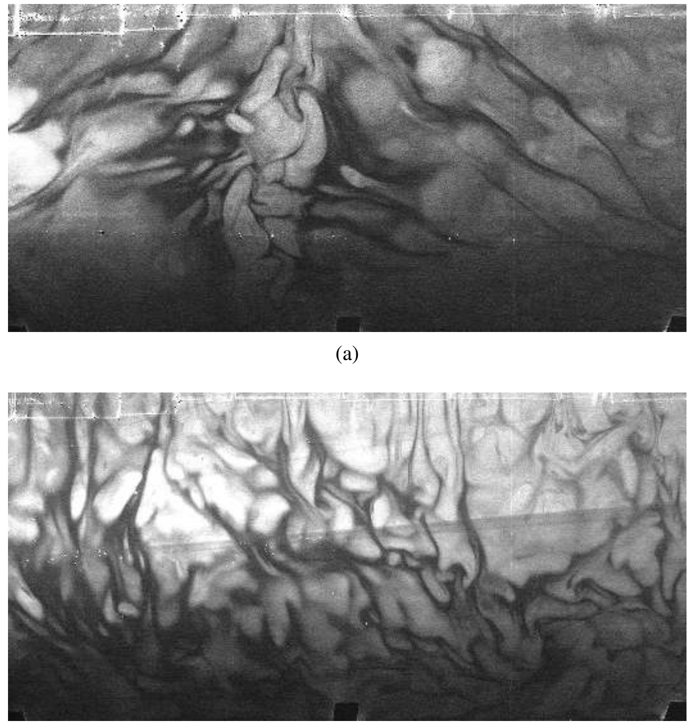
(a)
(b)

FIG. 5. Planforms of plume structure at approximately the same Re at two different Ra_w in MC in air; (a), $Re = 9.58 \times 10^3$ at $Ra_w = 5.75 \times 10^7$; (b), $Re = 9.6 \times 10^3$ at $Ra_w = 1.55 \times 10^8$. Flow is from top to bottom.

clearly seen.

B. Quantitative analysis of plume spacings

Figure(6) shows the variation of the mean plume spacing λ as a function of the shear velocity U_{sh} at different Ra_w in water and air. The hollow symbols show the variation of λ in air while the filled symbols show it in water. The same type of symbols indicates the same Ra_w. The solid line in the figure shows λ_0 for the no shear case at $Pr = 0.7$, evaluated using (1) at $Ra_w = 1.55 \times 10^8$, i.e. at the same Ra_w as $\triangle$. The dashed line shows λ_0 at $Pr = 5.09$ and $Ra_w = 6.03 \times 10^8$, corresponding to $\blacklozenge$. The figure also shows the values of λ measured from Gilpin et al. [17] at $Pr = 10.1$ and from Pirozzoli et al. [15] at $Pr = 1$. The error bars show the error in λ at some of the U_{sh}, estimated as discussed in II C.

The most noticeable feature of the figure is that the values of λ in air are about 4 to 5 times that in water, eventhough both are at around the same order of Ra_w, possibly because of the higher shear in air, which are about an order larger than that in water. Compared to the values in the no shear case, shown by the solid and the dashed lines in figure 6, shear increases the plume spacing to higher values; this increase from the no-shear values being lower in the lower Pr case. The low Pr data shows that at any Ra_w, shown by any of the hollow symbols in figure 6, shear increases λ. Further, the curves of each hollow

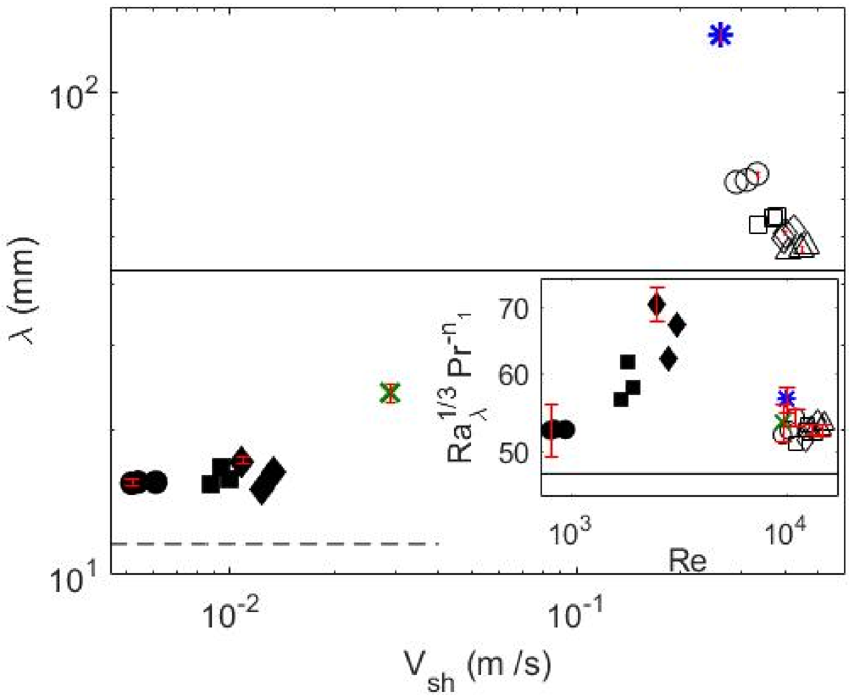

FIG. 6. (a)Variation of the mean plume spacing with the shear velocity. Hollow symbols indicate MC experiments in air at Pr = 0.7 for the following Ra_w. ○, $Ra_w = 5.75 \times 10^7$; □, $Ra_w = 1.01 \times 10^8$............... Filled symbols indicate RBC experiments in water for the following Ra_w and Pr. ●, $Ra_w = 1.09 \times 10^8$, $Pr = 5.24$; ■,.................; ×, MC experiments by Gilpin et al.[17] in water at $Pr = 10.1$ and $Ra_w = 2.17 \times 10^9$; ✳, MC simulations by Pirozzoli et al. [15] at $Pr = 1$ and $Ra_w = 5 \times 10^7$; ----, λ_0 given by (1) for $Ra_w = 6.03 \times 10^8$and $Pr = 5.09$; ——, λ_0 given by (1) for $Ra_w = 1.55 \times 10^8$and $Pr = 0.7$. The inset shows the variation of the dimensionless plume spacing with Reynolds number; ——, $Ra_{\lambda_0}^{1/3} Pr^{-n_1} = 47.5$ (3). (Pl.complete)

symbol move down with increase in Ra_w, implying that an increase in Ra_w at around similar shear reduces λ strongly at low Pr. Similar trends are also shown by the higher Pr data, but the increase of λ with shear seems to be much smaller here, possibly since the values of shear itself are small. Further, the increase of shear in these RBC experiments is accompanied by an increase of Ra_w also, since the large scale flow strength scales as $Ra_w^{4/9}$[4], which, as we saw above, has the effect of reducing the spacings. The decrease of λ with Ra_w, seen in the low Pr case cannot be seen for water, possibly since this decrease is offset by the increase in λ due to shear. The spacing in Pirozzoli et al. [15], at similar U_{sh} as that in air, seems to be disproportionately higher than those in air, since Ra_w is only slightly lower and Pr slightly higher in this case compared to air. In the case of Gilpin et al.[17], Ra_w is an order larger than those in water, which should have reduced λ compared to those in water. The observed contrary behaviour could be due to the increase of U_{sh}, and possibly Pr.

The above trends can be seen better in the variation of $\lambda/(Z_w Pr^{n_1}) = Ra_\lambda^{1/3}/Pr^{n_1}$, the dimensionless plume spacing with the dimensionless shear velocity, Re, shown in the inset in figure 6. The error bars in the figure show the estimated error in $Ra_\lambda^{1/3} Pr^{-n_1}$, calculated using the errors in ΔT_w and λ. For the case of no shear, as per (1), $Ra_{\lambda_0}^{1/3}/Pr^{n_1} = 47.5$, which is shown as the solid line in the inset. Since the vertical offset of the water data from the solid line is much more than that in the case of air, even when the shear velocity is much smaller in water, the effect of shear to increase λ over its no shear value λ_0 is seen to be much more in water compared to that in air. An increase in Pr seems to reduce the increase in λ with shear since the data of Gilpin et al. [17], which at $Pr = 10.1$ is at a much higher Re than our water data, does not show as much increase of λ over the corresponding no shear values. On the contrary, the data of Pirozzoli et al. [15], which is at almost the same Ra_w and Re as our air data, but at slightly higher Pr, shows an increase of λ compared to that in water. The increase of $Ra_\lambda^{1/3}$ with Re at any Pr seems to have the same trend at all Ra_w, even though this dependence does not seem to be any simple power law. The decrease in λ with Ra_w at the same shear, observed in the main figure, is also seen in the inset figure, where the values of $Ra_\lambda^{1/3}$ move down with increase in Ra_w, more prominently for air, than in water. Clearly, the variation of λ with shear shows quite a complex dependence on Re, Ra_w and Pr; we now present a scaling analysis which account for this non-trivial dependence.

C. Scaling of mean plume spacing with shear

1. Stability condition

Castaing et al [27] showed that in the presence of shear, the gravitational instability of natural convection boundary layers gets modified to result in a critical boundary layer thickness, given by

$$Ra_c^{bl} = A + B{Re_c^{bl}}^2, \tag{6}$$

where $Ra_c^{bl} = g\beta\Delta T_w\delta^3/\nu\alpha$ is the critical Rayleigh number based on the critical thermal boundary layer thickness δ at which the boundary layer becomes unstable, $Re_c{}^{bl} = U_{sh}\delta/\nu$ is the critical Reynolds number based on δ with $A(Pr)$ and $B(Pr)$ being unknown functions of Prandtl number. We define $\tilde{\delta} = \delta/Z_w$ and a shear parameter

$$S = \frac{U_{sh}^3\alpha}{g\beta\Delta T_w\nu^2} = \frac{1}{Ra_{sh}} = \frac{Re^3}{Ra_w} = \left(\frac{Z_w}{Z_{sh}}\right)^3, \tag{7}$$

which indicates the relative strength of shear with respect to buoyancy and dissipative effects, where the Rayleigh number based on the viscous-shear length Z_{sh},

$$Ra_{sh} = \frac{g\beta\Delta T_w Z_{sh}^3}{\nu\alpha}, \text{ with } Z_{sh} = \frac{\nu}{U_{sh}}. \tag{8}$$

Equation (6) can now be rewritten in terms of $\tilde{\delta}$ and S as

$$BS^{2/3}\tilde{\delta}^2 - \tilde{\delta} + A = 0. \tag{9}$$

Solving (9), we obtain

$$\frac{\delta}{\lambda} = \left(\frac{A}{Ra_\lambda}\right)^{1/3} + \frac{B}{3}\left(\frac{S^2}{Ra_\lambda}\right)^{1/3} + \frac{B^2}{9A^{1/3}}\left(\frac{S^4}{Ra_\lambda}\right)^{1/3} + O(S^2)\text{terms}. \tag{10}$$

We now assume that

$$\delta/\lambda = CPr^n \tag{11}$$

for small shear. This assumption implies that δ and λ have the same functional dependence on Ra_w and Re so that their ratio becomes only a function of Pr. Such is the case for plume spacings with no shear, as has been shown by [5], where both λ and δ scale as $C_iZ_wPr^{n_i}$, with different values of C_i and n_i for λ and δ, so that their ratio scale as CPr^n. We expect the same to occur in the presence of small shear; as we show later, this assumption accounts for the variation of λ in the present range of shear. Using (11) in (10) and neglecting terms with power of S greater than one, which is again valid for small shear, we obtain,

$$\left(\frac{A}{Ra_\lambda}\right)^{1/3} + \frac{B}{3}\left(\frac{S^2}{Ra_\lambda}\right)^{1/3} = CPr^n. \tag{12}$$

For $S \to 0$, i.e with no shear, $\lambda \to \lambda_0$ and $Ra_\lambda \to Ra_{\lambda_0}$, for which, (12) should tend to the corresponding no-shear relation (3),which implies that

$$A = C^3Pr^{3n}Ra_{\lambda_0}. \tag{13}$$

2. Scaling of excess plume spacings with shear.

Substituting (13) in (12), and rearranging, we obtain the difference of the plume spacing in the presence of shear from its no-shear value, $\lambda^* = \lambda - \lambda_0$, normalised by the viscous-shear length Z_{sh} (8), to scale as

$$\frac{\lambda^*}{Z_{sh}} = \frac{S}{D}, \tag{14}$$

where $D(Pr) = 3CPr^n/B$. Figure 7 shows the variation of $D\lambda^*/Z_{sh}$ with S in our experiments in air and water as well as for those measured from [17] and [15]. The error bars show the estimated error in $D\lambda^*/Z_{sh}$ and in S at some of the values of S, calculated from the possible errors in ΔT_w, λ and U_{sh} discussed in § II. The complex dependence of λ on Ra_w, Re and Pr, seen in figure 6, now collapse on to a common, simple, linear dependence of $D\lambda^*/Z_{sh}$ on S, in agreement with (14), when we use the variation

$$D = 52.7Pr^{-2.8}, \tag{15}$$

for $Pr < 5$, and

$$D = 0.004Pr^3 \tag{16}$$

for $Pr > 5$ shown in the inset. The decreasing and the increasing strong power law dependences of λ^* on Pr, for $Pr < 5$ and $Pr > 5$ repectively, could be because the thermal and velocity boundary layers cross over at $Pr \sim 1$.

The relation (14) can also be rewritten as

$$\frac{\lambda^*}{H} = \frac{1}{D}\frac{Re^2}{Ra_w}, \tag{17}$$

showing that λ^* scales as Re^2 and as $1/Ra_w$. Analogous to (3) for the case of no shear, (14) can also be rewritten in terms of Rayleigh and Reynolds numbers based on λ^* as

$$\frac{Ra_{\lambda^*}}{Re_{\lambda^*}^2} = \frac{1}{D}. \tag{18}$$

3. Scaling of ratio of plume spacings.

The ratio of plume spacing with shear to that without shear λ/λ_0 can be obtained from (14) to scale as

$$\frac{\lambda}{\lambda_0} = 1 + ES^{2/3} \tag{19}$$

where,

$$E(Pr) = \frac{1}{DC_1Pr^{n_1}}. \tag{20}$$

Figure 8 shows the variation of $(\lambda/\lambda_0 - 1)/E$ with the shear parameter S, using the values of E calculated using (15) and (16). The solid line shows the variation predicted by (19) with the error bars at some of the S showing the estimated errors in $(\lambda/\lambda_0 - 1)/E$ and S, calculated from the possible errors in

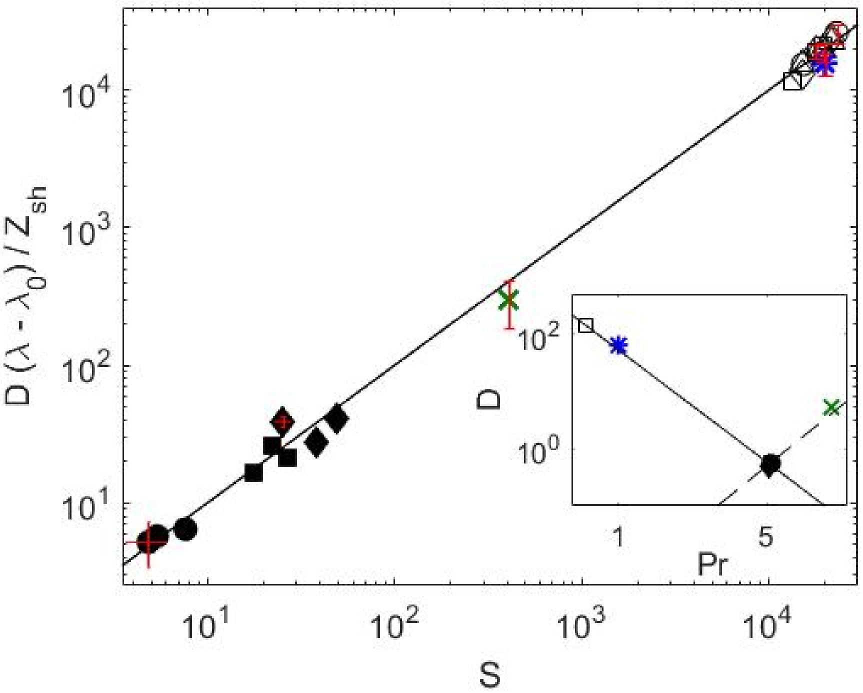

FIG. 7. Variation of λ^*, the difference of the mean plume spacing with shear (λ) from the corresponding no-shear values (λ_0), normalised by the viscous-shear length Z_{sh} (8), with the dimensionless shear parameter S (7); The symbols are as per figure 6 and table I; ——, (14). The inset shows the variation of the prefactor D in (14) with Pr; ——, (15); ---- , (16).

ΔT_w, λ and U_{sh}. The figure shows that the ratios of plume spacings with and without shear over the range of Ra_w, Re and Pr in our study obey the relation (19). Using (7), (15) and (16) in (19), we obtain

$$\frac{\lambda}{\lambda_0} = 1 + 4 \times 10^{-4} Pr^{2.7} \left(\frac{Re}{Ra_w^{1/3}}\right)^2, \text{ for } Pr < 5 \tag{21}$$

and

$$\frac{\lambda}{\lambda_0} = 1 + 5.36 Pr^{-3.1} \left(\frac{Re}{Ra_w^{1/3}}\right)^2, \text{ for } Pr > 5. \tag{22}$$

Expressions (21) and (22) show that the ratio of plume spacings λ/λ_0 at all Pr scale as $(Re/Ra_w^{1/3})^2$, but the spacings increase with Pr for $Pr < 5$ while they decrease with Pr for $Pr > 5$, presumably due to the cross over of the thermal and velocity boundary layers at $Pr \sim 1$.

4. *Scaling of length of plumes with shear*

Since $L_p = A/\lambda$ from (5), the above relations for λ also result in expressions for the total length of plumes on the surface in the presence of shear, analogous to the relations for the plume lengths L_{p_0} in the absence of shear, given by Puthenveettil et al.[5]. The left hand side of (14), after dividing by λ, can be rewritten as L_p^*/L_{p_0}, where $L_p^* = L_{p_0} - L_p$ is the reduction in plume length with shear from the no shear values. Using (19) to replace the λ on the right hand side, results that

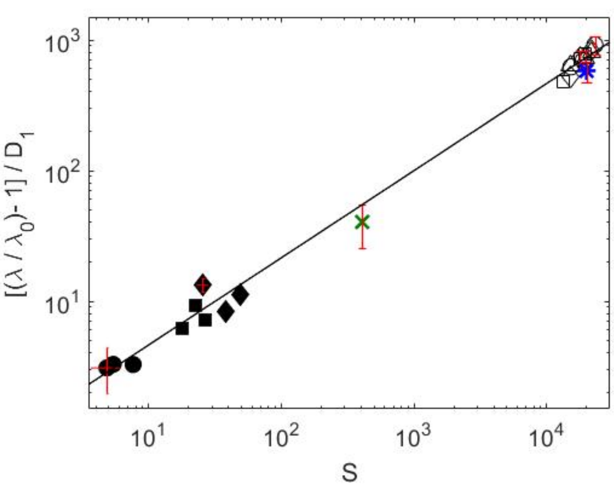

FIG. 8. Variation of the ratio of mean plume spacing with shear with the corresponding no-shear values with the dimensionless shear parameter S (7). The symbols are as per figure 6 and table I; ——, (19).

the ratio of the reduction in plume length with shear to the plume length in the absence of shear,

$$\frac{L_p^*}{L_{p_0}} = \frac{ES^{2/3}}{1 + ES^{2/3}}. \tag{23}$$

Similarly, since $\lambda/\lambda_0 = L_{p0}/L_p$ in (19), the ratio of plume lengths with shear to that without shear

$$\frac{L_p}{L_{p_0}} = \frac{1}{1 + ES^{2/3}}. \tag{24}$$

5. Upper limit of the present analysis

If we continue the above analysis without dropping the last term of order $S^{4/3}$ in (10), we obtain

$$\frac{\lambda}{\lambda_0} = 1 + ES^{2/3} + E^2 S^{4/3}. \tag{25}$$

The present analysis is then valid when the last term in (25) is small compared to the previous term, i.e. when

$$S < \frac{1}{E^{3/2}}. \tag{26}$$

Using the values of E from (20), with D given by (15) and (16) we obtain the upper limits of the present analysis as $S < 5.32 \times 10^5$ for $Pr = 0.7$, $S < 1.25 \times 10^5$ for $Pr = 1$, $S < 183.24$ for $Pr = 5.24$ and $S < 3.87 \times 10^3$ for $Pr = 10.1$. All these limits are above the range of the present data for the corresponding Pr.

IV. DISCUSSION AND CONCLUSIONS

The primary contribution of the present work is the scaling of plume spacings (λ) on the hot surface in turbulent Rayleigh Benard Convection (RBC) in the presence of internally generated shear, as well as in mixed convection (MC), where the shear is externally supplied. The difference of λ with the corresponding plume spacing in the absence of shear (λ_0), $\lambda^* = \lambda - \lambda_0$ is shown to scale as $\lambda^* = SZ_{sh}/D$ (14), where $S = Re^3/Ra_w$ is a dimensionless shear parameter that shows the relative strength of shear with respect to buoyancy and dissipative effects (7) and D a function of Pr (15), (16). Such a scaling implies that $\lambda^* = Z_w^3/Z_{sh}^2 D$, a function of two length scales near the plate, namely Z_w, the buoyancy-dissipative length scale (2) and Z_{sh}, the viscous-shear length (8).

The above scaling also means that, analogous to the relation $Ra_{\lambda_0}^{1/3} = 47.5 Pr^{0.1}$ for plume spacing without shear (3), the plume spacings in the presence of shear are given by $Ra_{\lambda^*}/Re_{\lambda^*}^2 = 0.02 Pr^{2.8}$ for $Pr < 5$ and by $Ra_{\lambda^*}/Re_{\lambda^*}^2 = 250 Pr^{-3}$ for $Pr > 5$, (18), where the subscript λ^* indicates that the dimensionless numbers are based on λ^*. We expect the positive and negative exponents of Pr in these relations for $Pr < 5$ and $Pr > 5$ to occur because the thermal and velocity boundary layers cross over at $Pr \sim 1$. The dimensionless excess plume spacing in the presence of shear then scales as $\lambda^*/H \sim Re^2/(DRa_w)$ (17). These relations, when written in terms of the ratio of plume spacings in the presence of shear with those with no-shear, imply that $\lambda/\lambda_0 \sim Pr^{2.7}(Re/Ra_w^{1/3})^2$ for $Pr < 5$, (21) and as $\lambda/\lambda_0 \sim Pr^{-3.1}(Re/Ra_w^{1/3})^2$ for $Pr > 5$, (22). All of these relations for λ also give rise to corresponding relations (23) and (24) for the length of plumes L_p that form on hot surfaces in RBC and MC.

These scalings of the plume spacings with shear were obtained by measuring the mean plume spacing from two types of experiments, as well as from two earlier studies by Gilpin et al [17] and Pirozzoli et al. [15]. Visualisations of the plume structure on the hot plate in steady, turbulent, mixed convection in air, which was forced externally by a shear, gave λ at $Pr = 0.7$. Plumes detected from PIV vector fields, using the horizontal divergence criterion[25], from the shear dominant regions in steady, turbulent, Rayleigh Benard convection in water gave λ at $5.09 < Pr < 5.24$. Measurements of λ from these two experiments, along with those from [17] and [15], together provided the variation of λ over one order of Ra_w and Re over $0.7 < Pr < 10.1$ to enable us to obtain the above scaling of the plume spacings. These experiments showed that, shear makes the line plumes aligned along the shear direction with λ increasing with shear for a given fluid and Ra_w. Correspondingly, for a given fluid at the same Re, an increase in Ra_w reduced the spacing. In addition, the spacings also had a non-monotonous dependence on Pr. These complex dependencies of the plume spacings in turbulent convection with shear on Ra_w, Re and Pr were succesfully captured by the above discussed scaling laws.

The above scaling laws, were obtained from the instability condition given by Castaing et al. [27] for natural convection boundary layers forced by shear, using the assumption that the ratio of critical boundary layer thickness and the plume spacing is only a function of Pr, after neglecting terms in the stability condition that had a power of S greater than one. The proposed scaling laws for the spacings are hence likely to hold only for small shear, given by upper limits of S, for each Pr; these limits were found to be $S = 184$ for $Pr = 5.24$ and $S = 5.31 \times 10^5$ for $Pr = 0.7$. At larger shear, forced convection effects would become predominant, with the flux scaling showing the standard relations for forced convection[13]. The evolution of the spacings beyond the present range of shear towards the forced convection limit needs to be investigated.

[1] O. Shishkina and C. Wagner, Phys. Fluids **19** (2007).

[2] L. Pera and B. Gebhart, Intl J.Heat Mass Transfer **16**, 1147 (1973).

[3] T. Haramina and A. Tilgner, Phys. Rev. E **69** (2004).

[4] B. A. Puthenveettil and J. H. Arakeri, J. Fluid Mech. **542**, 217 (2005).

[5] B. A. Puthenveettil, G. S. Gunasegarane, Y. K. Agrawal, D. Schmeling, J. Bosbach, and J. H. Arakeri, J. Fluid Mech. **685** (2011).

[6] S. A. Theerthan and J. H. Arakeri, Phys. Fluids **12**, 884 (2000).

[7] S. A. Theerthan and J. H. Arakeri, J. Fluid Mech. **373**, 221 (1998).

[8] J. Bosbach, S. Weiss, and G. Ahlers, Physical review letters **108**, 054501 (2012).

[9] S. Grossman and D. Lohse, J. Fluid Mech. **407**, 27 (2000).
[10] N. Shi, M. S. Emran, and J. Schumacher, Journal of Fluid Mechanics **706**, 5 (2012).
[11] M. van Reeuwijk, H. J. J. Jonker, and K. Hanjalic, Phys. Rev. E **77**, 036312 (2008).
[12] X. Wang, Journal of Heat Transfer **104**, 139 (1982).
[13] F. Incropera, A. Knox, and J. Maughan, Journal of heat transfer **109**, 434 (1987).
[14] H. Imura, R. Gilpin, and K. Cheng, Journal of Heat Transfer **100**, 429 (1978).
[15] S. Pirozzoli, M. Bernardini, R. Verzicco, and P. Orlandi, Journal of Fluid Mechanics **821**, 482516 (2017).
[16] G. S. Gunasegarane and B. A. Puthenveettil, J. Fluid Mech. **749**, 37 (2014).
[17] R. R. Gilpin, H. Imura, and K. C. Cheng, Trans. ASME Jl. of Heat transfer **100**, 71 (1978).
[18] A. Garai, J. Kleissl, and S. Sarkar, Journal of Fluid Mechanics **757**, 57 (2014).
[19] R. J. Adrian, Physics of Fluids **19**, 041301 (2007).
[20] S. Lyons, T. Hanratty, and J. McLaughlin, AIChE journal **35**, 1962 (1989).
[21] R. Falco, Phil. Trans. R. Soc. Lond. A **336**, 103 (1991).
[22] R. R. Gilpin, H. Imura, and K. C. Cheng, Journal of Heat Transfer **100(1)**, 71 (1978).
[23] G. Ahlers, S. Grossman, and D. Lohse, Rev. Mod. Phys **81**, 503 (2009).
[24] B. Wieneke, Measurement Science and Technology **26**, 074002 (2015).
[25] K. Vipin and B. A. Puthenveettil, in *Proceedings of the* 8^{th} *world conference on experimental heat transfer, fluid mechanics and thermodynamics, Lisbon* (2013).
[26] E. Sparrow and R. Husar, Journal of Fluid Mechanics **37**, 251 (1969).
[27] B. Castaing, G. Gunaratne, F. Heslot, L. Kadanoff, A. Libchaber, S. Thomae, X.-Z. Wu, S. Zaleski, and G. Zanetti, Journal of Fluid Mechanics **204**, 1 (1989).